Design of the Attitude Estimation Algorithms for the GT-1 CubeSat

Nelson G. Guecha-Ahumada* and E. Glenn Lightsey†
Georgia Institute of Technology, Atlanta, GA, 30332

GT-1 is the first of four 1U CubeSats under development by the Georgia Institute of Technology's Space Systems Design Laboratory (SSDL). Its main objective is to prove the feasibility of an inexpensive spacecraft bus designed and fabricated by students in just over a year. Given the mass, volume and cost constraints; the sensor suite is limited to low-cost Commercial-Off-The-Shelf (COTS) components such as Coarse Sun Sensors, a Magnetometer, an Inertial Measurement Unit (IMU), and a Global Positioning System (GPS) receiver. A 6-Degree-of-Freedom (6-DOF) simulation of GT-1 was created to develop sensor models and estimation algorithms. Two static attitude determination methods, TRIAD and Davenport's Q-Method were developed and evaluated using the 6-DOF simulation. In addition, an Extended Kalman Filter (EKF) was developed using the same simulation environment to provide a sequential attitude estimation framework capable of propagating the attitude dynamics and correcting the attitude estimate. This document acts as a survey of reliable attitude estimation techniques and algorithms that can be implemented on an elementary mission profile based on a modest sensor suite.

I. Nomenclature

Symbols

A	=	attitude transformation matrix
a_i	=	q-method weight associated to sensor i
B	=	attitude profile matrix
$\hat{\boldsymbol{b}}$	=	unit vector of attitude reference in body frame
$\boldsymbol{d}$	=	vector from the spacecraft to the Sun
$F(t)$, $M(t)$, $Q(t)$	=	kalman filter propagation matrices
$G(\cdot)$	=	q-method gain function
H	=	sensitivity matrix
$\boldsymbol{h}(\hat{\boldsymbol{x}})$	=	sensor estimate output
$\boldsymbol{I}_j$	=	light intensity at Sun sensor j
I_{max}	=	maximum sunlight intensity
$J(\cdot)$	=	minimization cost function
K	=	kalman gain matrix
$L(\cdot)$	=	q-method loss function
$\mathbf{N}$	=	vector of sensor measurement errors
$\hat{\boldsymbol{n}}_j$	=	unit vector normal to sensor j
P	=	state error covariance matrix
$\boldsymbol{q}$	=	quaternion
$\hat{\boldsymbol{q}}$	=	unit quaternion
R	=	measurement error covariance matrix
$\hat{\boldsymbol{r}}$	=	unit vector of attitude reference in known frame
$\hat{\boldsymbol{s}}$	=	unit vector from the spacecraft to the Sun
$\boldsymbol{V}$	=	vector of Sun sensor output voltages
$\hat{\boldsymbol{v}}$	=	TRIAD unit vectors computed from reference frame
W	=	weight matrix

*Graduate Student, Daniel Guggenheim School of Aerospace Engineering, ngga3@gatech.edu. AIAA Student Member
†Professor, Daniel Guggenheim School of Aerospace Engineering, glenn.lightsey@gatech.edu. AIAA Fellow

$\hat{\boldsymbol{w}}$	=	TRIAD unit vectors computed from body frame
$\hat{x}$	=	state estimate
$\mathbf{Y}$	=	vector of sensor measurement outputs
$\tilde{\boldsymbol{y}}$	=	sensor measurement output
$Z, D(B)$	=	auxiliary matrices used in the q-method
$\boldsymbol{\beta}$	=	angular rate bias
$\hat{\boldsymbol{\beta}}$	=	estimated angular rate bias
$\delta\alpha$	=	approximated euler angle error
$\Delta\hat{x}$	=	error-state update
$\Delta\boldsymbol{\beta}$	=	bias estimate update
$\boldsymbol{\eta}_u$	=	zero-mean Gaussian process noise of rate gyro bias rate
$\boldsymbol{\eta}_v$	=	zero-mean Gaussian rate gyro process noise
λ	=	eigenvector
$\boldsymbol{\nu}$	=	vector of Sun sensor measurement errors
σ	=	standard deviation
ϕ, θ, ψ	=	rotation angles used in the euler angle sequence
$\Xi(\boldsymbol{q})$	=	4×3 matrix created from quaternion $\boldsymbol{q}$
$\boldsymbol{\omega}$	=	true angular rate
$\tilde{\boldsymbol{\omega}}$	=	measured angular rate
$\hat{\boldsymbol{\omega}}$	=	estimated angular velocity

Acronyms

ADCS	Attitude Determination and Control System
COTS	Commercial Off-The-Shelf
CSS	Course Sun Sensor
EKF	Extended Kalman Filter
FOV	Field Of View
GPS	Global Positioning System
ISS	International Space Station
LEO	Low Earth Orbit
PSD	Position Sensitive Detector

II. Introduction and Motivation

CubeSats are becoming a popular method for space exploration due to their fast fabrication times and relatively inexpensive components, allowing greater production volumes at a fraction of the cost of standard satellites. Furthermore, continuous advances in microelectronics have made CubeSats an effective alternative as space sensing platforms to their full-size counterparts. Nowadays university groups design, test and assemble nanosatellites that oftentimes become secondary payloads of flagship missions. To date, the Space Systems Design Laboratory (SSDL) at Georgia Tech has built and operated two satellite missions: RANGE A/B and PROX-1 [1]. These missions were launched on SpaceX rockets in 2018 and 2019 respectively. Besides the technical challenges present in satellite development, university groups face the additional setback of frequent shifts in student workforce due to the students' relatively short time-span in college. The GT 1-4 series is conceived to significantly reduce the design-to-fabrication time of a university satellite by taking advantage of a small form factor while simplifying mission complexity with the goal of creating a reliable spacecraft bus that can be delivered in roughly one year. Being the first in the series, the GT-1 mission bears the additional challenge of setting a strong foundation for the following three satellites. GT-1 adheres to the 1U CubeSat

standard, which entails that all satellite components are stowed within a volume of $10cm \times 10cm \times 10cm$ and with a total mass not to exceed 1.3 kg [2]. Each of these nanosatellites will be launched to the International Space Station (ISS). Once in the ISS, they will be deployed into a Low Earth Orbit (LEO) equivalent to the ISS orbit using a Poly-Picosatellite Orbital Deployer, or P-POD launcher. The satellite is expected to tumble right after deployment and attitude acquisition shall be performed autonomously during detumbling. Commands and telemetry will be sent and received using the ground station at Georgia Tech. The mission is limited to basic satellite operations which requires only the modest pointing requirements of wide beamwidth antennas.

Spacecraft attitude is the orientation of a satellite with respect to a known (typically inertial) frame of reference. Attitude determination becomes key in the space environment given that satellite operations may require precise pointing of an antenna and/or camera. Basic spacecraft attitude determination requires at least two non-collinear vectors from the spacecraft to a known reference. Two reference vectors commonly used by spacecraft at LEO are the Sun and the magnetic field direction at the satellite's location. The Sun and magnetic field vectors can be determined using Sun sensors and magnetometers respectively. Other common sensors include star trackers which compute the spacecraft's attitude based on a star catalog and horizon sensors which estimate a planet's centroid to determine the spacecraft's pitch and roll angles. Given two non-collinear vector references, static attitude determination methods can be used to provide a rough estimate of the satellite's pointing in real time. The validity of attitude estimates is limited to the reliability of the sensors, which are themselves susceptible to measurement noise and natural physical phenomena that impact their performance. Examples of these phenomena include the effect of Earth albedo on Sun sensors or the loss of the Sun reference during eclipse (very common in LEO). More robust attitude estimation methods can be used to overcome several of these challenges. For instance, sequential estimation techniques produce a statistically optimal attitude estimate by taking advantage of the system dynamics to propagate the attitude states and the measurements to correct the attitude prediction. The Extended Kalman Filter (EKF) is a commonly used sequential estimation algorithm applicable to nonlinear systems such as the attitude estimation problem [3].

This report is intended as a survey of the most relevant attitude estimation algorithms for the GT-1 mission starting from the sensor suite design and simulation of sensor models. The performance of multiple estimation techniques is evaluated to provide valuable insight for GT-1 flight software engineers. The reliability of the attitude estimate is limited to the sensor performance and precise pointing operations may not be feasible using modest Commercial-Off-The-Shelf (COTS) sensors. Consequently, a future work section is included to address sensor development and additional recommendations for the upcoming GT CubeSat series missions.

III. Sensor Selection

The volume, mass and cost constraints drive the sensor suite design of the GT-1 Attitude Control and Determination System (ADCS). In addition, reliable sensors with flight heritage are preferred due to the limited time between mission concept, fabrication, and assembly. Satellites in LEO rely on multiple vector references such as the magnetic field of Earth, the Sun, Earth horizon, and other stars. A minimum of two independent non-collinear references are needed to produce an attitude estimate. Satellite developers have found that Coarse Sun Sensors (CSS) and a three-axis magnetometer have the potential to produce a reliable attitude estimate using inexpensive and flight proven components [3–5]. Two additional auxiliary sensors are also recommended: A Global Positioning System (GPS) receiver to track the satellite position and a rate gyroscope to measure the spacecraft body rotational rates. A general overview of the technical characteristics recommended sensors follows.

A. Sun Sensors

Two types of sensors are used to determine the Sun vector: Analog or Coarse Sun Sensors (CSS) and fine or Digital-fine Sun Sensors (DSS). The CSS are photodiodes that produce an electric current proportional to the incoming light intensity. Sunlight intensity varies with the incidence angle between the Sun and the sensor. As a result, the incidence angle can be estimated thus providing one of the three components of the Sun vector. Three non-parallel CSS measurements can be combined to produce a Sun vector estimate. DSS are more accurate and are capable of producing a Sun vector measurement with a single sensor; however, DSS are more complex and expensive (in the order of thousands of dollars). After taking these factors into consideration, the Osram SFH-2430 CSS were selected for their wide field of view, ease of use, low-cost and flight heritage. The Osram CSS is shown in figure 1 and its most relevant technical characteristics are included in table 1.

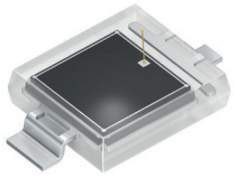

Fig. 1 SFH 2430 Coarse Sun Sensor [6]

Table 1 Technical characteristics of the Osram SFH 2430 Photodiodes [6]

Characteristic	Value
Wavelength of Peak Sensitivity	570 nm
Spectral Range of Sensitivity	400-900 nm
Half-Angle	Field of View: 60°

B. Three-axis Magnetometer

Magnetometers are used to measure the local magnetic field in the satellite body frame. If the spacecraft position is known, the reference magnetic field vector at the spacecraft's location can be computed using the International Geomagnetic Reference Field (IGRF). An attitude vector reference results from the combined knowledge of the measured magnetic field in the satellite reference frame and the IGRF defined magnetic field at the satellite's location. The Honeywell HMC 1053 magnetometer is a low cost and versatile sensor selected for the GT-1 mission. Table 2 includes the most relevant performance characteristics of this magnetometer.

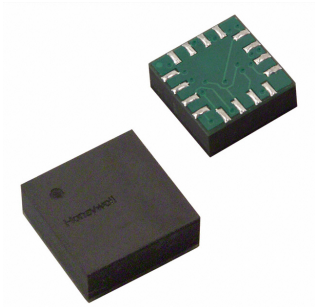

Fig. 2 HMC 1053 Magnetometer [7]

C. GPS Receiver

Precise spacecraft positioning is required for satellite tracking and for generating a reliable attitude reference using the magnetometer. The dual-frequency OEM615 was selected to communicate with the GPS constellation and determine the position and velocity of the CubeSat. Standard GPS are capable of a position accuracy of a few meters and a velocity accuracy in the order of tens of cm/s [8].

D. Inertial Measurement Unit (IMU)

IMU are used to measure triaxial angular body rates and acceleration of spacecraft. None of these measurements can be compared against a reference frame, therefore they cannot provide an external attitude reference. However, advanced attitude estimation techniques such as Kalman filters use spacecraft body rates and attitude references to produce an optimal attitude estimate [9]. The M-G354PDCA EPSON IMU was chosen due to its small form factor and relatively high stability. The IMU is sensitive to 6 degrees of freedom, three of which correspond to the rate gyro and three to the accelerometer. The IMU's technical characteristics are shown in table 3:

Table 2 Technical characteristics of the HMC 1053 Magnetometer [7]

Characteristic	Value
Field Range	+/-6 gauss
Sensitivity	0.8 to 1.2 mV/V/gauss
Resolution	120 μgauss
Bandwidth	5 MHz

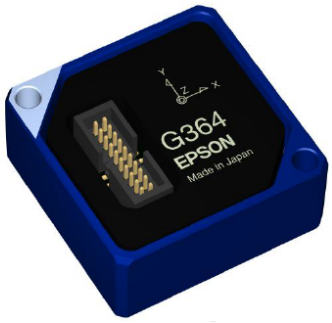

Fig. 3 EPSON M-G354PDCA IMU [10]

IV. Simulation Models

This section of the document presents an overview of the sensor simulation models. The main constraints and assumptions used in the development of the three presented sensor models are included.

A. Sun Sensor Model and Sensor Placement

Basic Coarse Sun Sensor (CSS) models treat the Sun as a point source. The light intensity of a point source can be modelled with the following expression:

$$\boldsymbol{I}_j = \begin{cases} I_{max}(\hat{\boldsymbol{n}}_j \cdot \hat{\boldsymbol{s}}) & for \quad \hat{\boldsymbol{n}}_j \cdot \hat{\boldsymbol{s}} > 0 \\ 0 & for \quad \hat{\boldsymbol{n}}_j \cdot \hat{\boldsymbol{s}} \leq 0 \end{cases} \tag{1}$$

where $\hat{\boldsymbol{n}}_j$ is a unit vector normal to the sensor and $\hat{\boldsymbol{s}}$ is a unit vector in the direction from the spacecraft to the Sun [11]. This expression ignores the CSS field of view (FOV). Equation 1 can be modified to take into account the limited line of sight of the CSS as follows:

$$\boldsymbol{I}_j = \begin{cases} I_{max}(\hat{\boldsymbol{n}}_j \cdot \hat{\boldsymbol{s}}) & for \quad \hat{\boldsymbol{n}}_j \cdot \hat{\boldsymbol{s}} > 0 \quad \& \quad \hat{\boldsymbol{n}}_j \cdot \hat{\boldsymbol{s}} \leq \cos(FOV) \\ 0 & otherwise \end{cases} \tag{2}$$

The models previously described do not account for light intensity noise. In practice, CSS are subject to noise from multiple sources. The most significant light intensity noise source for spacecraft in LEO is Earth albedo which can pull the CSS output off from the true Sun direction up to 20° [11]. Earth albedo models have been developed to mitigate the

Table 3 Technical characteristics of the EPSON M-G364PDCA IMU [10]

Characteristic	Value
Gyro Dynamic Range	100-200 deg/s
Gyro Bias Instability	2.2 deg/s
Gyro Angular Random Walk	0.09 deg/$\sqrt{hr}$
Accelerometer Dynamic Range	+/- 3G
Accelerometer Bias Instability	0.05 mG

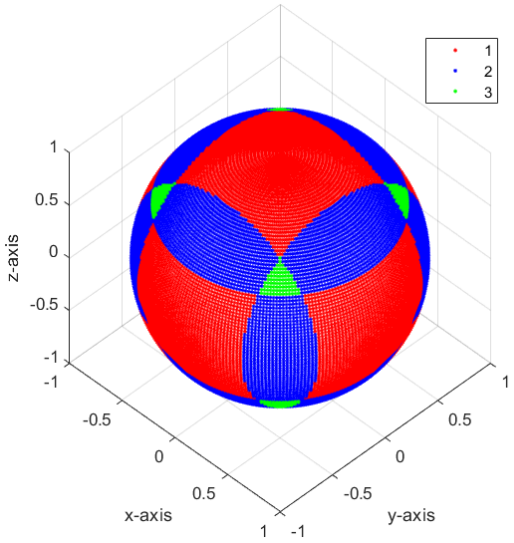

Fig. 4 Six CSS coverage

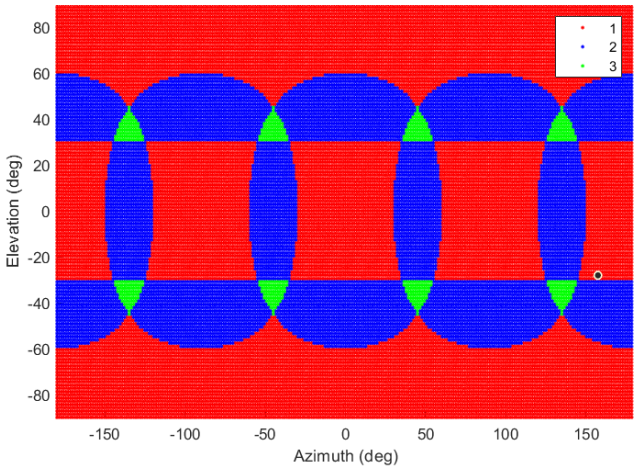

Fig. 5 Mercator projection of 6 CSS coverage

effects of albedo noise on Sun sensors [4, 5]. Earth albedo models have not been developed for the GT-1 CubeSat in order to streamline the flight software complexity and decrease the development time. Earth albedo models should be considered for subsequent CubeSat missions if precise pointing is required using modest sensors.

The number of CSS and the location and orientation of each sensor is of important consideration due to the FOV limitations. Maximum sensor coverage is desired with the minimum number of CSS due to the cost, mass and volume constraints. A tool to facilitate Sun sensor placement and orientation was developed to aid in the CSS design. Multiple CSS with varying pointing directions were studied using this tool and a baseline configuration of 6 CSS was selected (see figures 4 and 5). 6 CSS with a FOV of 55° distributed at each of the six faces of the 1U CubeSat ensure that the spacecraft is always in view of the Sun unless it is in eclipse [12]. The Osram SFH-2430 CSS has a FOV of 60°; therefore, six CSS (one on each face) would always be in view when the spacecraft is not in eclipse and up to three CSS can be in view simultaneously.

Once in orbit, the GT-1 CubeSat will deploy four solar panels as shown on figure 6. Deployable solar panels can improve power generation, but at at the same time, they are likely to block incoming sunlight on the CSS adjacent to the deployed panel. The CSS placement tool was adapted to adjust the FOV of CSS adjacent to a deployable solar panel. Results are shown on figure 7. Sunlight blockage due to a deployable depends on the length of the face where the CSS is placed (10 cm for 1U) and the distance between the CSS and the deployable's hinge. The loss in effective FOV is minimized by placing the CSS at the greatest distance from the hinge. The current test case assumes that the CSS is located at the greatest distance possible from the deployable solar panel hinge (10 cm for 1U). Results show that the effective FOV decreased to 52.5° for the four CSS located at shaded faces; as a result, four small sections of the coverage sphere, that originally detected the Sun with three CSS, cannot receive sunlight anymore. This test case showcases the best CSS coverage possible with the current deployable solar panel configuration and six CSS. It is expected that the actual performance will change (and likely worsen) after the CSS are assembled to the structure, but the actual location can be input to the shaded CSS placement tool to generate the expected FOV.

Since the precise CSS location is still to be determined, the standard 6 CSS cube configuration is assumed for the rest of the document. A single CSS can only determine one component of the three-component Sun vector; likewise, two CSS are not sufficient to completely determine the orientation of the Sun. The Sun must be in view of three CSS mounted in different orientations to calculate the Sun vector. This fact represents a major challenge due to the volume constraints of the CubeSat and the non-trivial integration of multiple CSS at various angles [3]. The limitations of CSS can be overcome through the implementation of advanced attitude determination methods such as Kalman Filters. These algorithms allow satellite developers to combine CSS measurements with magnetometer data (and any other attitude reference sensor) and measured spacecraft body rates to produce a more reliable attitude estimate [3, 11]. An alternative method to potentially maximize Sun sensor coverage without increasing the number of sensors consists of using solar panels as "Coarse Sun Sensors". In principle CSS and solar panels are equivalent since the energy

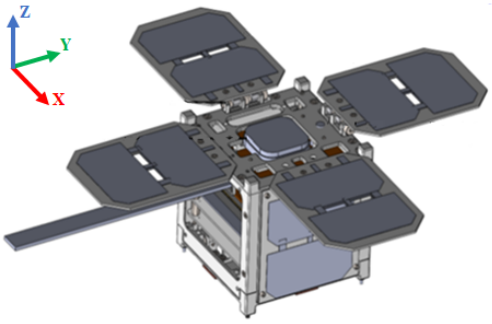

Fig. 6 GT-1 deployed configuration

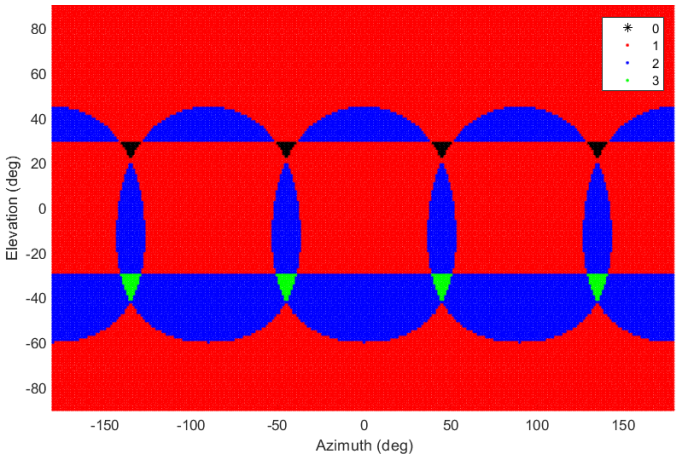

Fig. 7 6 CSS coverage accounting for solar panel shading

produced by the sunlight depends on the incidence angle between the Sun and the solar panel. Methods to utilize solar panel outputs to generate a Sun vector estimate have been developed in the past; however, these methods pose further challenges on hardware development and reliability [13]. Least-squares and minimum-norm techniques are simple and reliable alternatives to generate a Sun vector estimate from a limited number of CSS detector outputs. These methods are explored in the following section.

B. Magnetometer Model

Magnetic field models have been a subject of research for decades. These models use similar mathematical techniques used for gravity field models such as spherical harmonics for the magnetic potential [11]. However, magnetic forces are are not exclusively attractive; repulsive forces are also present (represented by North and South poles). Crassidis' magnetic field model algorithm was used due to the platform compatibility and code heritage [14]. The main inputs to this algorithm are the satellite position and measurement time. The magnetic field order can also be varied to allow researchers to generate "true" measurements (high-order) and coarse measurements (low-order). The GT-1 simulation implements true magnetic field and magnetometer readings using 10th and 6th degree order models respectively. The International Geomagnetic Reference Field (IGRF) is maintained by multiple agencies and updated every five years. The current simulation uses the 2015-2019 IGRF coefficients. Future missions should ensure that the IGRF coefficients are updated to the 2020-2025 release.

C. Rate Gyroscope Model

Angular rates are typically measured using a rate-integrating gyro. A widely used model of this sensor follows from the first order Markov process [15] summarized as follows:

$$\boldsymbol{\omega} = \tilde{\boldsymbol{\omega}} - \boldsymbol{\beta} - \boldsymbol{\eta}_v \tag{3}$$

$$\dot{\boldsymbol{\beta}} = \boldsymbol{\eta}_u \tag{4}$$

Where $\boldsymbol{\eta}_v$ and $\boldsymbol{\eta}_u$ are zero-mean Gaussian white-noise processes with spectral density $\sigma_v^2 I_{3\times3}$ and $\sigma_u^2 I_{3\times3}$ respectively, $\boldsymbol{\beta}$ is a bias vector, and $\tilde{\boldsymbol{\omega}}$ is the measured observation. The estimated angular velocity is given by [11]

$$\hat{\boldsymbol{\omega}} = \tilde{\boldsymbol{\omega}} - \hat{\boldsymbol{\beta}} \tag{5}$$

V. Attitude Estimation Techniques

This section explores several estimation techniques possible with the selected sensor configuration. Theoretical foundations of various static and sequential attitude determination techniques are presented. The performance of each algorithm was evaluated using a 6-Degree-of-Freedom (6-DOF) simulation and results are presented in this section.

A. Static Attitude Determination

1. Least Squares-Minimum Norm (LS-MN)

The least squares technique can be used to produce a Sun vector estimate from three or more CSS measurements. This process is deterministic and can generate an sun vector estimate as long as at least three CSS are in view of the Sun. This technique consists of minimizing the CSS measurement errors $(\nu_1, \nu_2, ..., \nu_N)$.

$$\begin{bmatrix} V_1 \\ \vdots \\ V_N \end{bmatrix} = \begin{bmatrix} \hat{\boldsymbol{n}}_1 \\ \vdots \\ \hat{\boldsymbol{n}}_N \end{bmatrix} \boldsymbol{d} + \begin{bmatrix} \nu_1 \\ \vdots \\ \nu_N \end{bmatrix} \tag{6}$$

On the expression above, V_i is the output voltage and $\boldsymbol{d}$ is the unnormalized sun vector. In other words, the Sun vector can be computed by $\hat{s} = \frac{\boldsymbol{d}}{\|\boldsymbol{d}\|}$. In addition $\|\boldsymbol{d}\|$ can be used as a calibration parameter equivalent to the Sun intensity. Equation 6 can be rearranged in terms of matrices as follows:

$$\boldsymbol{Y} = H\boldsymbol{x} + \boldsymbol{N} \tag{7}$$

where $\boldsymbol{Y}$ is a vector of CSS output voltages, H is the mapping matrix or matrix with CSS locations with respect to the spacecraft body frame, $\boldsymbol{x}$ is the state vector (here $\boldsymbol{x} = \mathbf{d}$), and $\boldsymbol{N}$ is a vector of measurement errors to minimize. The cost function for this minimization problem can be expressed as

$$J_{LS}(\boldsymbol{x}) = \frac{1}{2}\boldsymbol{\nu}^T\boldsymbol{\nu} = \frac{1}{2}(\boldsymbol{Y} - H\boldsymbol{x})^T(\boldsymbol{Y} - H\boldsymbol{x}) \tag{8}$$

if three or more measurements are available and the output is normalized, the least squares solution gives [12]

$$\hat{\boldsymbol{x}} = (H^T H)^{-1} H^T \boldsymbol{Y} \tag{9}$$

in the case that only 1 or 2 CSS are in view, then the minimum norm technique can be used to produce a rough estimate of the Sun vector for the under-determined system [12]

$$\hat{\boldsymbol{x}} = H^T (HH^T)^{-1} \boldsymbol{Y} \tag{10}$$

The least squares-minimum norm (LS-MN) estimation algorithms were implemented to a simulated satellite with six CSS (one CSS per face of the cube). The Sun input is generated from all possible Azimuth and Elevation angles and the angle error (in degrees) between the resulting Sun vector estimate and the true Sun vector is calculated in the absence of noise. Figure 8 shows that, theoretically, the angle error is zero when three CSS are in view (see figure 5). The error increases when less than 3 CSS are in view and reaches a value up to 60° when the Sun is at the edge of the field of view of one CSS. The over-determined case occurs when more than 3 CSS are simultaneously in view of the Sun, but such arrangement is not possible under the current CSS configuration. However, the LS-MN algorithm supports any number of CSS and orientations. Simulations of over-determined configurations (more than 3 CSS on view) gave an angle error of zero degrees identical to the three CSS case; moreover, an over-determined configuration would likely perform better in practice. In reality, CSS are also subject to noise due to Earth albedo and imperfections within the CSS (which could be mitigated through sensor calibration). The current simulation did not capture any of these effects. One way to enhance the LS-MN algorithm and partially account for Earth albedo effects consists of including a weight matrix in the least squares minimization process

$$J_{WLS}(\boldsymbol{x}) = \frac{1}{2}\boldsymbol{\nu}^T \boldsymbol{W}\boldsymbol{\nu} = \frac{1}{2}(\boldsymbol{Y} - H\boldsymbol{x})^T W(\boldsymbol{Y} - H\boldsymbol{x}) \tag{11}$$

the normalized state estimate results in the classic weighted least squares solution [12]

$$\hat{\boldsymbol{x}} = (H^T H)^{-1} H^T W\boldsymbol{Y} \tag{12}$$

where W is a diagonal weight matrix that is set to the CSS output measurements so that strong outputs from sensors in view of the Sun are favored over weaker outputs that are likely to be due to Earth albedo noise [12].

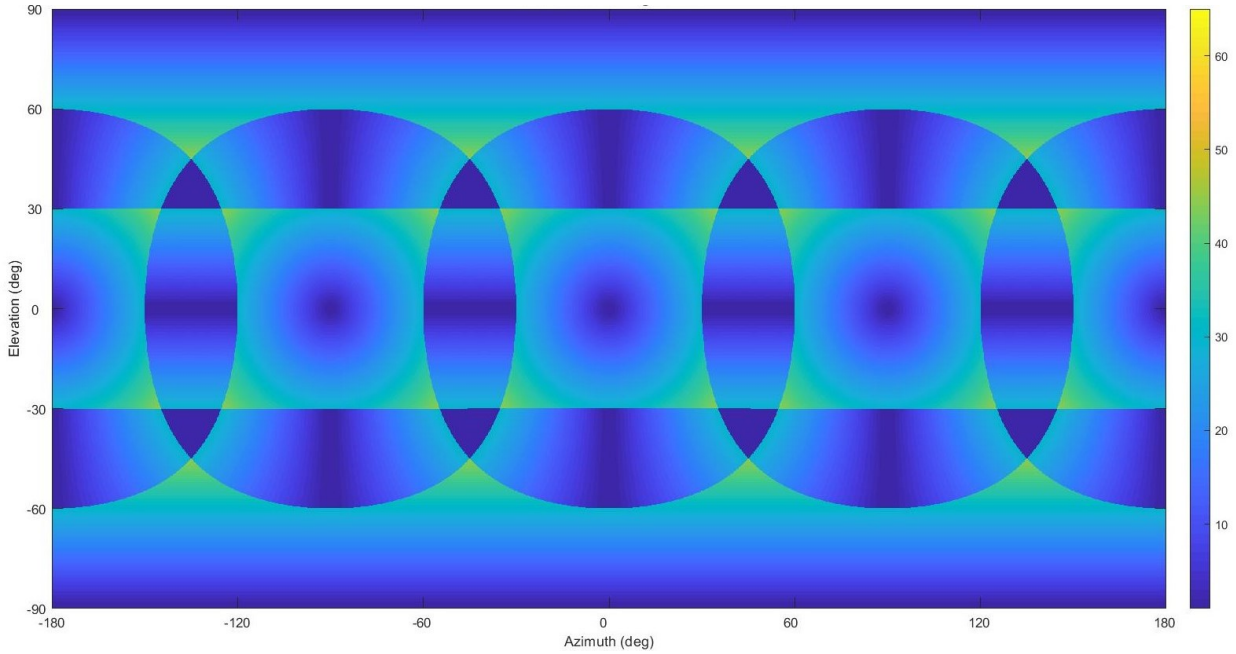

Fig. 8 Six CSS cube arrangement LS-MN output error in degrees

2. TRIAD

The Tri-Axial Attitude Determination technique (TRIAD) is capable of generating a satellite attitude estimate from two vector measurements. This is achieved by assuming that the two measurements are also known in some reference frame (N). The overall goal is to compute a transformation matrix $A_{[BN]}$ that rotates the vectors from a reference frame (N) to the spacecraft body frame (B) [11]:

$$A_{[BN]}\hat{\boldsymbol{r}}_i = \hat{\boldsymbol{b}}_i, \qquad for \qquad i = 1, 2 \tag{13}$$

Where $\hat{\boldsymbol{r}}_{1,2}$ are two reference unit vectors in a known reference frame and $\hat{\boldsymbol{b}}_{1,2}$ are the same reference unit vectors measured in the body frame. This expression above implies that the following is also true:

$$\hat{\boldsymbol{b}}_1 \cdot \hat{\boldsymbol{b}}_2 = (A_{[BN]}\hat{\boldsymbol{r}}_1) \cdot (A_{[BN]}\hat{\boldsymbol{r}}_2) = \hat{\boldsymbol{r}}_1^T A_{[BN]}^T A_{[BN]}\hat{\boldsymbol{r}}_2 = \hat{\boldsymbol{r}}_1 \cdot \hat{\boldsymbol{r}}_2 \tag{14}$$

In general equation 14 is only true for error-free measurements. In practice, both inequalities are impossible to satisfy. The TRIAD method implies that one of the measured unit vectors (say $\hat{\boldsymbol{b}}_1$) is more accurately known and is selected as the main reference $\hat{\boldsymbol{w}}_1$ for the new TRIAD frame (T). A secondary unit vector orthogonal to the first $\hat{\boldsymbol{w}}_2$ is created by taking the cross product of the main sensor measurement with the secondary sensor measurement. The third vector of the auxiliary frame $\hat{\boldsymbol{w}}_3$ is a unit vector orthogonal to $\hat{\boldsymbol{w}}_1$ and $\hat{\boldsymbol{w}}_2$.

$$\hat{\boldsymbol{w}}_1 = \hat{\boldsymbol{b}}_1, \qquad \hat{\boldsymbol{w}}_2 = \hat{\boldsymbol{b}}_\times \equiv \frac{\hat{\boldsymbol{b}}_1 \times \hat{\boldsymbol{b}}_2}{\left\|\hat{\boldsymbol{b}}_1 \times \hat{\boldsymbol{b}}_2\right\|}, \qquad \hat{\boldsymbol{w}}_3 = \hat{\boldsymbol{b}}_1 \times \hat{\boldsymbol{b}}_\times \tag{15}$$

The unit vectors $\hat{\boldsymbol{w}}_{1:3}$ correspond to the column unit vectors for a transformation from the TRIAD frame to the body frame $[BT]$. A similar procedure produces the column unit vectors for a transformation from the TRIAD frame to the reference frame $[NT]$:

$$\hat{\boldsymbol{v}}_1 = \hat{\boldsymbol{r}}_1, \qquad \hat{\boldsymbol{v}}_2 = \hat{\boldsymbol{r}}_\times \equiv \frac{\hat{\boldsymbol{r}}_1 \times \hat{\boldsymbol{r}}_2}{\|\hat{\boldsymbol{r}}_1 \times \hat{\boldsymbol{r}}_2\|}, \qquad \hat{\boldsymbol{v}}_3 = \hat{\boldsymbol{r}}_1 \times \hat{\boldsymbol{r}}_\times \tag{16}$$

As mentioned, the rotation matrices from the TRIAD frame to the body and reference frames can be constructed using $\hat{\boldsymbol{w}}_{1:3}$ and $\hat{\boldsymbol{v}}_{1:3}$ respectively:

$$A_{[BT]} = [\hat{\boldsymbol{w}}_1 \quad \hat{\boldsymbol{w}}_2 \quad \hat{\boldsymbol{w}}_3], \qquad A_{[NT]} = [\hat{\boldsymbol{v}}_1 \quad \hat{\boldsymbol{v}}_2 \quad \hat{\boldsymbol{v}}_3] \tag{17}$$

A Direction Cosine Matrix (DCM) that relates the body frame to the reference frame can be computed as follows [16]:

$$A_{[BN]} = A_{[BT]} A_{[NT]}^T \tag{18}$$

In the absence of errors, the resulting DCM produces a perfect orthogonal mapping. In practice, the actual DCM is subject to measurement errors. The resulting DCM can be used to compare the true (uncorrupted) attitude matrix $A_{[BN]_{true}}$ and the computed (corrupted) attitude matrix $A_{[BN]}$.

Overall, TRIAD is capable to produce an attitude estimate from two vector measurements known in the body and the known reference frames. However, it is limited to two attitude references and any additional independent attitude inputs cannot be processed simultaneously. Furthermore, the two vector inputs to the TRIAD algorithm must not be parallel or anti-parallel since the cross products, shown in equations 16 and 17, would become zero and lead to a singularity. In other words, the two sensor inputs would act as a single sensor measurement.

3. Davenport's Q-Method

Davenport's Q-method extends beyond the capabilities of the TRIAD algorithm by processing more than two sensor measurements to perform attitude estimations. Originally, this problem was formulated mathematically in 1965 by Grace Wahba. Wahba's Problem consists of finding the orthogonal matrix A with determinant equal to 1 that minimizes the loss function [11]

$$L(A) = \frac{1}{2} \sum_{i=1}^{N} a_i \left\| \hat{\boldsymbol{b}}_i - A\hat{\boldsymbol{r}}_i \right\|^2 \tag{19}$$

where $\hat{\boldsymbol{b}}_i$ is a set of N unit vectors measured in the spacecraft body frame, $\hat{\boldsymbol{r}}_i$ are the corresponding unit vectors in a reference frame, and a_i are the weights assigned to each sensor. Paul Davenport provided the first solution of this problem applicable for spacecraft attitude determination [11] by employing quaternions:

$$\boldsymbol{q} = [q_0 \quad q_1 \quad q_2 \quad q_3]^T \tag{20}$$

Wahba's loss function can be rewritten as follows:

$$L(A) = \frac{1}{2} \sum_{i=1}^{N} a_i (\hat{\boldsymbol{b}}_i - A\hat{\boldsymbol{r}}_i)^T (\hat{\boldsymbol{b}}_i - A\hat{\boldsymbol{r}}_i) \tag{21}$$

$$L(A) = \frac{1}{2} \sum_{i=1}^{N} a_i (\hat{\boldsymbol{b}}_i^T \hat{\boldsymbol{b}}_i + \hat{\boldsymbol{r}}_i^T \hat{\boldsymbol{r}}_i - 2\hat{\boldsymbol{b}}_i^T A\hat{\boldsymbol{r}}_i) \tag{22}$$

$$L(A) = \sum_{i=1}^{N} a_i (1 - \hat{\boldsymbol{b}}_i^T A\hat{\boldsymbol{r}}_i) \tag{23}$$

without loss of generality, equation 23 is equivalent to maximizing the gain function $G(\cdot)$ [16]

$$G(A) = \sum_{i=1}^{N} a_i \hat{\boldsymbol{b}}_i^T A\hat{\boldsymbol{r}}_i \tag{24}$$

the rotation matrix A can be rewritten in terms of quaternions (Euler parameters) using equation 25

$$A = (q_0^2 - \boldsymbol{q}_{1:3}^T \boldsymbol{q}_{1:3}) I_{3\times 3} + 2\boldsymbol{q}_{1:3}\boldsymbol{q}_{1:3}^T - 2q_0[\tilde{\boldsymbol{q}}_{1:3}] \tag{25}$$

where q_0 is equivalent to the rotation angle (scalar component of quaternion) and $\boldsymbol{q}_{1:3}$ is the unit vector along the axis of rotation (vector component of quaternion). The term $[\tilde{\boldsymbol{q}}_{1:3}]$ is a skew symmetric matrix constructed using the vector components of $\boldsymbol{q}$. The gain function $G(\cdot)$ can now be rewritten using the 4×4 symmetric traceless matrix (trace is zero) $D(B)$, where B is known as the "attitude profile matrix":

$$G(\boldsymbol{q}) = \boldsymbol{q}^T D(B) \boldsymbol{q} \tag{26}$$

$$D(B) = \begin{bmatrix} trB & Z^T \\ Z & B + B^T - (trB) I_{3\times 3} \end{bmatrix}, \qquad B \equiv \sum_{i=1}^{N} a_i \hat{\boldsymbol{b}}_i \hat{\boldsymbol{r}}_i^T \tag{27}$$

$$Z = \begin{bmatrix} B_{23} - B_{32} \\ B_{31} - B_{13} \\ B_{12} - B_{21} \end{bmatrix} = \sum_{i=1}^{N} a_i(\hat{\boldsymbol{b}}_i \times \hat{\boldsymbol{r}}_i) \tag{28}$$

The gain function (equation 26) cannot be solved directly due to the unit length constraint of quaternions. Lagrange multipliers can instead be used to yield a new function $G'(\cdot)$:

$$G'(\boldsymbol{q}) = \boldsymbol{q}^T D(B)\boldsymbol{q} - \lambda(\boldsymbol{q}^T \boldsymbol{q} - 1) \tag{29}$$

the expression above can be differentiated and set equal to zero to find the extrema of this function:

$$\frac{d}{d\boldsymbol{q}}(G'(\boldsymbol{q})) = 2D(B)\boldsymbol{q} - 2\lambda\boldsymbol{q} = 0 \quad \Rightarrow \quad D(B)\boldsymbol{q} = \lambda\boldsymbol{q} \tag{30}$$

the desired quaternion is an eigenvector of the $K(B)$ matrix. The G function can be maximized by selecting the largest eigenvalue of the $K(B)$ matrix.

$$G(\boldsymbol{q}) = \boldsymbol{q}^T D(B)\boldsymbol{q} = \boldsymbol{q}^T \lambda\boldsymbol{q} = \lambda\boldsymbol{q}^T \boldsymbol{q} = \lambda \tag{31}$$

$$L(A(\boldsymbol{q})) = \lambda_0 - \lambda_{max}, \qquad \lambda_0 = \sum_{i=1}^{N} a_i \tag{32}$$

Finally, the quaternion (eigenvector) that corresponds to the selected eigenvalue can be plugged into equation 25 to compute the resulting transformation matrix $A_{[BN]}$.

4. 6-DOF Simulation Results

TRIAD and Davenport's Q-Method were implemented on a 6-DOF simulation of the GT-1 satellite in MATLAB®. As mentioned in the introduction, the GT-1 CubeSat will operate on an orbit similar to the ISS at an altitude of $\sim$ 400 km and an inclination of 51.6°. The prescribed satellite attitude is nadir pointing with the z-axis pointing to Earth, the x-axis pointing in the direction of motion and the y-axis completing the orthogonal system. The body frame orientation is as shown on figure 6. No environmental perturbations (i.e. solar, gravitational, aerodynamic, etc.) were included in the simulation. The simulated sensors include six CSS, a magnetometer, and a rate gyro. The true spacecraft quaternion and orbital elements are propagated with time and are post processed to produce raw sensor measurements after generating the nominal states. The transformation from the reference inertial frame to the body frame corresponds to the 3-1-3 Euler Angle Sequence $R_{313}(\phi, \theta, \psi) = R_3(\phi)R_1(\theta)R_3(\psi)$. The magnetic field simulator takes the satellite's position, epoch and the desired magnetic field order. A 10th degree order model is used for the reference magnetic field and a 6th degree order model is selected for the magnetometer along with zero-mean gaussian noise of σ = 50nT. In addition, the Sun ephemeris is propagated at each epoch and the vector from the satellite to the Sun is computed. Brief eclipse periods where no CSS is in-view of the Sun are also included in the simulation. The six CSS normal to each face are simulated (without added noise) and their output is processed using the LS-MN algorithm. Simulated sensor outputs from the magnetometer and the CSS are then used to run the TRIAD and the Q-Method algorithms. A simplified block diagram of the simulation is shown on figure 9.

Figure 10 shows the error in the TRIAD attitude estimate with the magnetometer as the primary sensor reference. Results show that the error ranges from $\sim$ 0° up to a maximum of 180°. The error spiked and/or reached the maximum value when the magnetic field and sun vector were aligned. Eclipse periods are also apparent at the portions where the TRIAD algorithm does not produce a solution since no CSS is in view of the Sun (the number of CSS in view at each epoch are shown in red). The current simulation has a maximum of two CSS in view, and for the majority of the simulation, only one or zero CSS are in view. Figure 8 shows that, in general, the attitude deviation from truth is lower when two CSS are in view than for a single CSS in view. This fact is partially confirmed through figure 10. On average, the TRIAD attitude estimate was found to be 33.77° off from truth.

The Q-Method estimation results are shown on figure 11. It can be seen that the resulting attitude errors has a shape similar to figure 10; however, the Q-Method had a worse performance than TRIAD since the resulting average attitude estimate error increased to 36.01°. This small decrease in performance can be explained by the fact that both sensors (CSS and magnetometer) were given equal weight during the Q-Method computations. The Q-Method average estimate error was decreased down to 33.77° when the magnetometer measurement weight was increased with respect to the CSS measurement weight. The current sensor configuration did not allow the Q-Method attitude estimate to improve the

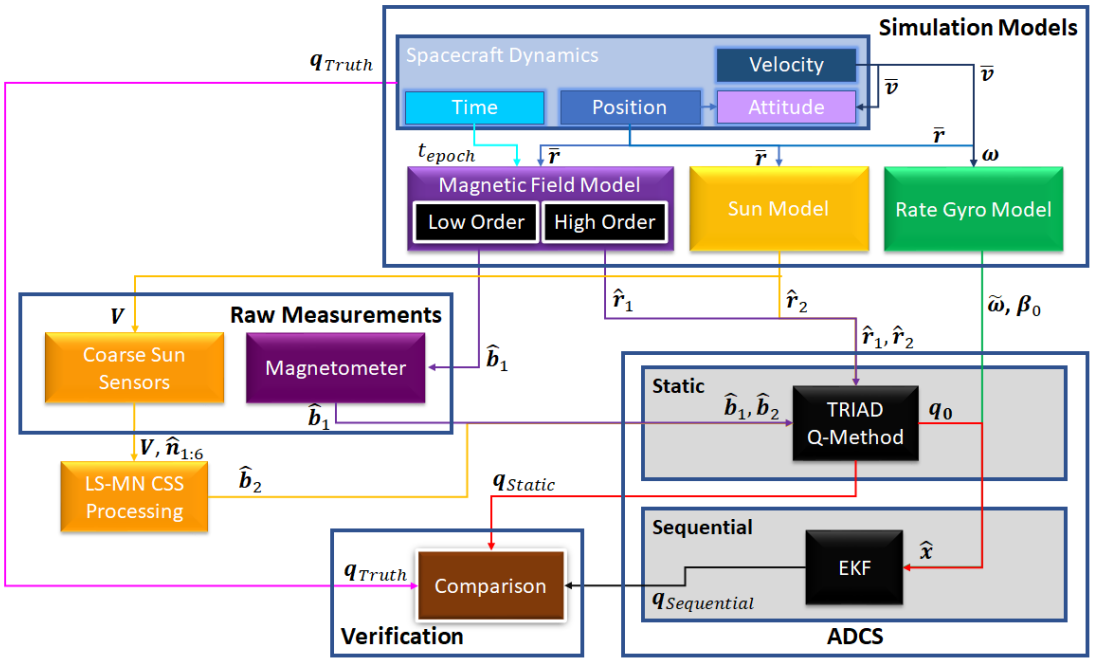

Fig. 9 Simulation block diagram

beyond the TRIAD estimate regardless of the choice of weights. The alignment between the Sun and the local magnetic field vector is included figure 11 for reference. Similar to the TRIAD attitude estimate, an alignment of the Sun vector with the local magnetic field vector produces a spike of the attitude estimate error in the Q-Method estimate.

Overall, the error in the attitude estimate depends on the number of CSS in view and the alignment between the magnetic field and the Sun vector. The GT-1 satellite does not have control over the number of CSS in view nor the alignment of the magnetic field and the Sun vector; however, the CubeSat could be programmed to make an "educated guess" on whether the static attitude estimate is reliable by ensuring that the magnetic field and the Sun vector are not aligned. This can be detected from the satellite's position (GPS output) along with the number of CSS in view at a given measurement time. The attitude estimate could also be improved by adding a third sensor to track another attitude reference (other than the Sun and the magnetic field). A third attitude reference would most likely eliminate the singularity caused during the Sun and magnetic field vector alignment; however, if three or more sensors are processed simultaneously, the static attitude determination process would be limited to the Q-Method (or similar algorithms).

B. Sequential Attitude Determination

Sequential attitude estimation techniques have the capability of simultaneously propagating state dynamics and correcting attitude estimates using attitude measurements combined with knowledge of the spacecraft body rates. Sequential estimators overcome the main disadvantages of single-point estimators such as the inability to produce an attitude estimate under the partial absence of measurements (i.e. eclipse conditions), or during singularities sue to attitude reference vector alignment. In other words, sequential estimation techniques may provide bounded and continuous attitude estimate errors.

1. Extended Kalman Filter (EKF)

The Kalman filter is used to produce a statistically optimal estimate of linear systems [11]. Nonlinear systems, such as the satellite attitude state propagation, can be estimated by implementing a Kalman filter to a linearization of the nonlinear system [17]. The Extended Kalman Filter (EKF) results from a first-order approximation of the state and observation equations about a reference trajectory [12]. EKF have widely been used on-board spacecraft and produce acceptable results under reliable initial conditions. Table 4 summarizes the EKF algorithm to estimate the quaternion and rate gyro bias. The state vector has a size of 7×1; however, the first-order approximation assumes that the true

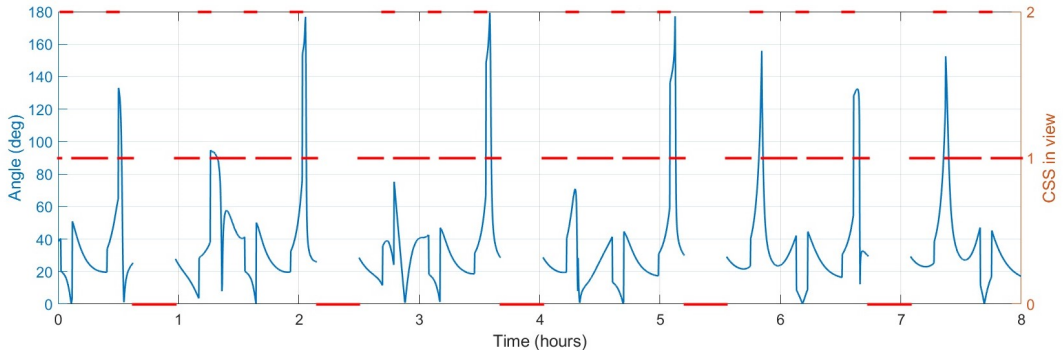

Fig. 10 TRIAD algorithm results

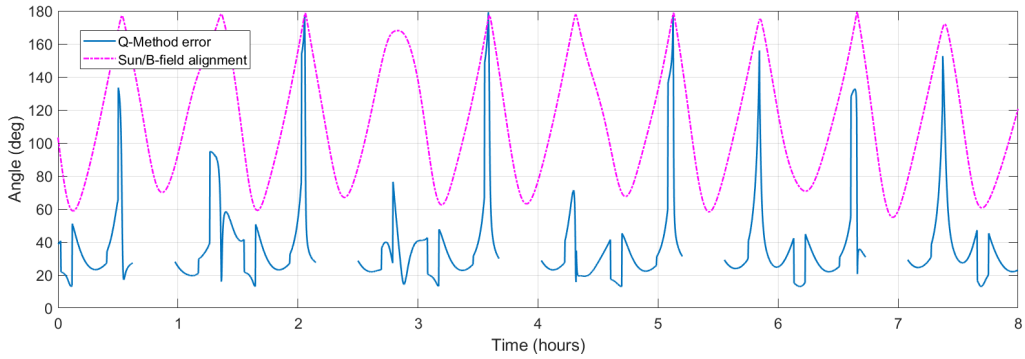

Fig. 11 Q-Method algorithm results

quaternion is "close" to the estimated quaternion. This allows the system to be reduced by one state. Overall, the EKF algorithm, shown in table 4, can be summarized as follows [9]:

The algorithm begins by initializing the filter with a known state (assuming zero initial bias) and an initial error covariance matrix ($P_0 : 6 \times 6$), where the first three diagonal elements of the matrix correspond to the initial error covariance of attitude and the last three elements correspond to the initial error covariance of gyro bias. The Kalman gain matrix K is computed using the measurement error covariance R and the sensitivity matrix $H_k(\hat{\boldsymbol{x}}_k^-)$. The update equations are then used to generate the new state error covariance P_k^+, the error-state update $\Delta\hat{\tilde{\boldsymbol{x}}}_k^+$, the bias $\hat{\boldsymbol{\beta}}_k^+$, and quaternion $\hat{\boldsymbol{q}}_k^+$ updates. At this point the quaternion is re-normalized by brute force $\hat{\boldsymbol{q}}^+ = \frac{1}{\left\|\hat{\boldsymbol{q}}^+\right\|}\hat{\boldsymbol{q}}^+$ and the estimated angular velocity $\hat{\omega}$, is used to propagate the quaternion kinematics model $\dot{\hat{\boldsymbol{q}}}(t)$ and standard error covariance $\dot{P}(t)$.

2. 6-DOF Simulation Results

The EKF algorithm was added to the same 6-DOF simulation used to test the static attitude determination algorithms (figure 9). The initial quaternion corresponded to the first quaternion estimate available from the Q-Method (the TRIAD quaternion estimate can also be used) and the initial state $\hat{\boldsymbol{x}}_0$ was completed assuming zero gyro bias. Once the filter is started, rate gyro measurements with noise are fed to the algorithm as the system propagates forward in the simulation. Figure 12 shows that the error in euler angles (ϕ, θ, ψ) is bounded throughout the simulation; however, it does not converge to zero as time increases. Figure 13 represents the overall attitude estimate error of the EKF output. The initial quaternion is off from the true quaternion by $\sim 38°$; however, the error decreased quickly as the simulation progresses. The attitude error shows periodic peaks that correspond to the alignment between the Sun and magnetic field vectors. Eclipse periods are highlighted in black to demonstrate that losing the Sun vector reference does not prevent the filter from propagating and converging to a solution. Instead, the error tends to decrease during eclipse periods, which can be attributed to the filter relying on physical models rather than measurements to perform state estimate corrections. The resulting average error of the EKF algorithm was $6.56°$, which is a large value for precise pointing applications, but acceptable for coarse pointing requirements such as communication with ground stations using a wide beam-width antenna.

Table 4 EKF equations for attitude estimation [9]

Initialize	$\hat{\boldsymbol{q}}(t_0) = \hat{\boldsymbol{q}}_0, \quad \hat{\boldsymbol{\beta}}(t_0) = \hat{\boldsymbol{\beta}}_0$ $P(t_0) = P_0$
Gain	$K_k = P_k^- H_k^T(\hat{\boldsymbol{x}}_k^-)\left[H_k(\hat{\boldsymbol{x}}_k^-)P_k^- H_k^T(\hat{\boldsymbol{x}}_k^-) + R\right]^{-1}$ $H_k(\hat{\boldsymbol{x}}_k^-) = \begin{bmatrix} \left[A(\hat{\boldsymbol{q}}^-)\hat{\boldsymbol{r}}_1 \times\right] & 0_{3\times3} \\ \vdots & \vdots \\ \left[A(\hat{\boldsymbol{q}}^-)\hat{\boldsymbol{r}}_n \times\right] & 0_{3\times3} \end{bmatrix}\Big\vert_{t_k}$ $R = diag\left[\sigma_1^2 I_{3\times3} \quad \sigma_2^2 I_{3\times3} \ldots \sigma_n^2 I_{3\times3}\right]$
Update	$P_k^+ = \left[I - K_k H_k(\hat{\boldsymbol{x}}_k^-)\right]P_k^-$ $\Delta\hat{\hat{\boldsymbol{x}}}_k^+ = K_k\left[\tilde{\boldsymbol{y}}_k - \boldsymbol{h}_k(\hat{\boldsymbol{x}}_k^-)\right]$ $\Delta\hat{\hat{\boldsymbol{x}}}_k^+ \equiv \left[\delta\hat{\boldsymbol{\alpha}}_k^{+T} \Delta\hat{\boldsymbol{\beta}}_k^{+T}\right]^T$ $H_k(\hat{\boldsymbol{x}}_k^-) = \begin{bmatrix} \left[A(\hat{\boldsymbol{q}}^-)\hat{\boldsymbol{r}}_1\right] \\ \left[A(\hat{\boldsymbol{q}}^-)\hat{\boldsymbol{r}}_2\right] \\ \vdots \\ \left[A(\hat{\boldsymbol{q}}^-)\hat{\boldsymbol{r}}_n\right] \end{bmatrix}\Big\vert_{t_k}$ $\hat{\boldsymbol{q}}_k^+ = \hat{\boldsymbol{q}}_k^- + \frac{1}{2}\Xi(\hat{\boldsymbol{q}}_k^-)\delta\hat{\boldsymbol{\alpha}}_k^+, \quad$ re-normalize quaternion $\hat{\boldsymbol{\beta}}_k^+ = \hat{\boldsymbol{\beta}}_k^- + \Delta\hat{\boldsymbol{\beta}}_k^+$
Propagation	$\hat{\boldsymbol{\omega}}(t) = \tilde{\boldsymbol{\omega}}(t) - \hat{\boldsymbol{\beta}}(t)$ $\dot{\hat{\boldsymbol{q}}}(t) = \frac{1}{2}\Xi(\hat{\boldsymbol{q}}(t))\hat{\boldsymbol{\omega}}(t)$ $\dot{P}(t) = F(t)P(t)F^T(t) + M(t)Q(t)M^T(t)$ $F(t) = \begin{bmatrix} -\left[\hat{\boldsymbol{\omega}}(t)\times\right] & I_{3\times3} \\ 0_{3\times3} & 0_{3\times3} \end{bmatrix}, \quad M(t) = \begin{bmatrix} -I_{3\times3} & 0_{3\times3} \\ 0_{3\times3} & I_{3\times3} \end{bmatrix}$ $Q(t) = \begin{bmatrix} \sigma_v^2 I_{3\times3} & 0_{3\times3} \\ 0_{3\times3} & \sigma_u^2 I_{3\times3} \end{bmatrix}$

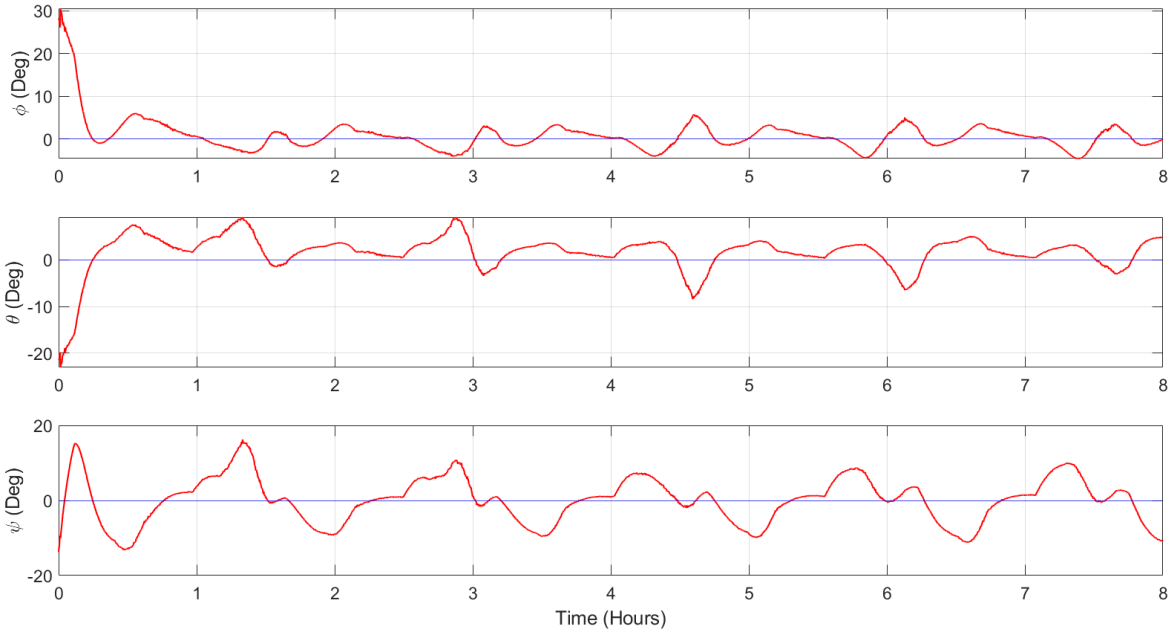

Fig. 12 Euler angle error (EFK)

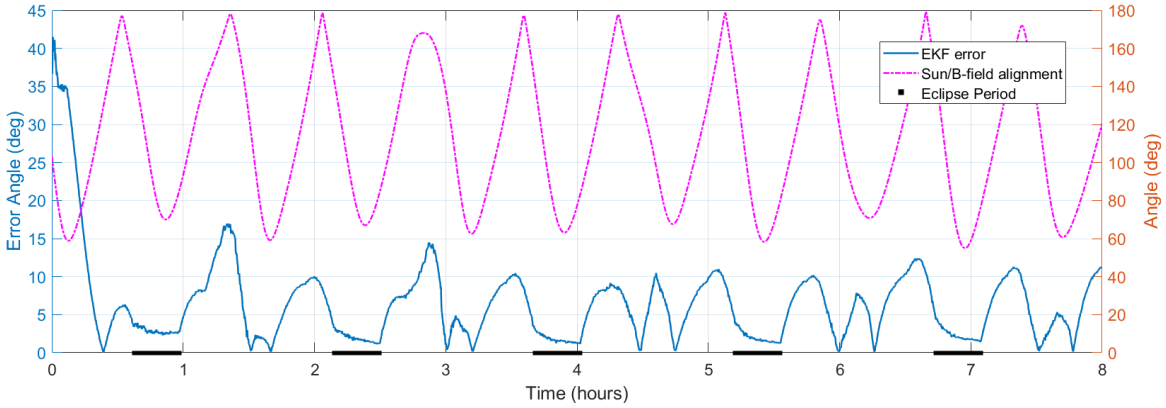

Fig. 13 Attitude estimate error (EFK)

VI. Conclusion

A modest attitude estimation suite for the GT-1 CubeSat was designed sensor by sensor, and modelled as a whole using a 6-DOF simulation of the satellite. The quantitative performance of the sensor suite was computed through the development and implementation of several attitude estimation algorithms for sensor processing.

A sensor suite of six Coarse Sun Sensors (CSS) and a Magnetometer including a GPS receiver is sufficient to produce an initial coarse attitude estimate within $\sim 30^\circ$ of truth when not in eclipse using TRIAD or Q-Method static estimation algorithms. A six CSS configuration with sensors distributed on each face of the CubeSat is able to continuously estimate the Sun vector reference (when not in eclipse), but it can be off from the Sun reference by up to 60° when only one CSS is in view. Furthermore, an alignment of the local magnetic field vector with the Sun vector has the net effect of eliminating one attitude reference and rendering attitude estimates unreliable. Fortunately, the number of CSS in view and the alignment between the Sun vector and local magnetic field vector could be determined on board the spacecraft. In other words, the flight computer logic could be programmed to indicate whether a coarse attitude estimate is reliable. In the current simulation, the quality of the initial static attitude estimate is limited by the capabilities of the CSS. In practice the reliability of each sensor should be determined through comprehensive hardware testing.

The addition of an IMU provides rate gyro measurements that were fed to an Extended Kalman Filter (EKF) along with the initial coarse attitude estimate produced by the static estimation algorithms. An initial attitude quaternion that differed from truth by $\sim 38^\circ$ was successful at starting the EKF and producing an attitude estimate error bounded within $\sim 10^\circ$ after 8 hours ($\sim$ 5 orbits). In the current simulation, eclipse periods did not have an adverse effect on the EKF estimate output; however, more realistic rate gyro performance parameters should be applied to study the actual behavior of the filter under eclipse conditions.

Overall, this report shows that the selected sensor suite and developed algorithms have the potential to allow a simple mission profile such as communicating with a ground station using an wide beam-width antenna. On the other hand, applications that require precise pointing and/or more complex mission profiles are most likely not achievable. The main limitation towards more ambitious spacecraft operations lies in the modest sensor suite selection. The addition of more sensors and replacing the current the course sensors with more robust alternatives has the potential to produce attitude estimates closer to the nominal after being processed by similar algorithms. However, a more robust attitude system would come at the expense of size, weight, power, cost, and development time.

VII. Future Work

This report has established that a 1U CubeSat attitude determination and control system is feasible using inexpensive and relatively simple COTS components. However, further development is recommended in the following areas to validate and verify the current models and to enhance the sensor hardware for upcoming missions.

A. Sensor Model Fidelity and Simulation Enhancement

The sensor models created/adapted for this study are simplified representations of the actual components. It is recommended that sensor models of increased fidelity be developed by either researching and implementing new robust models or adjusting the simulations to better represent the technical characteristics of the sensors. The models can be validated by comparing the behavior of sensor models against hardware on a bench-top configuration.

Similarly, the current 6-DOF simulation serves only as an initial development framework of the GT-1 satellite to test various sensor configurations and/or estimation algorithms. It is recommended that a more robust simulation of the GT-1 satellite be developed by simulating mission operations and more realistic environmental dynamics. Mission operations include control sequences and mission critical events such as communication passes and power system charge/discharge cycles. Furthermore, more realistic satellite dynamics can be represented by modeling miscellaneous (gravitational, aerodynamic, solar, etc.) perturbations and disturbance torques that would experience a CubeSat in LEO.

B. Custom Built Sun Sensor Using Position Sensitive Detectors (PSD)

This report demonstrated the limitations of CSS detectors at measuring the Sun vector. Digital Sun Sensors (DSS) are a reliable alternative to CSS; however, their cost escalates over thousands of dollars. DSS have been developed through the implementation of Position Sensitive Detectors (PSD). Multiple universities have taken advantage of this fact to develop their own "customized" DSS [18] at a fraction of their retail cost. This section of the document summarizes the design and development of a customized low-cost and small-factor DSS previously developed by university satellite developers.

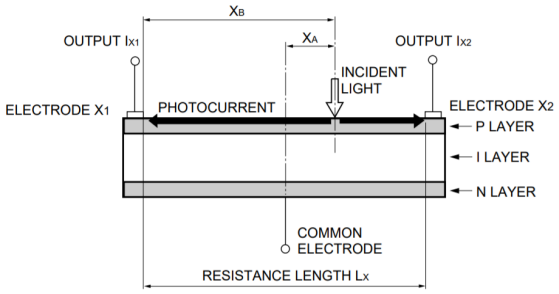

Fig. 14 PSD sectional view [19]

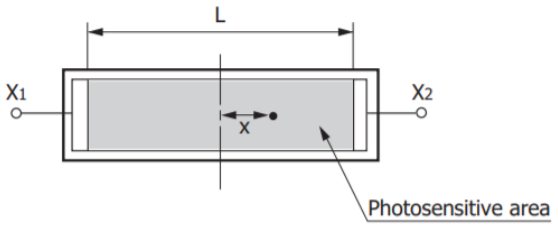

Fig. 15 PSD top view [20]

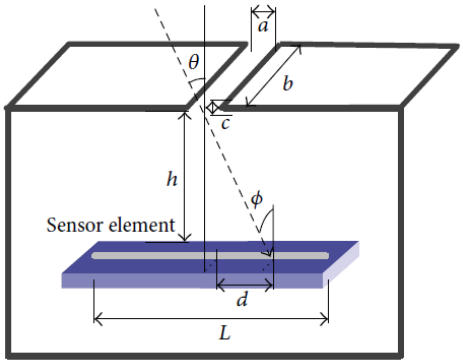

Fig. 16 One-dimensional PSD slit [22]

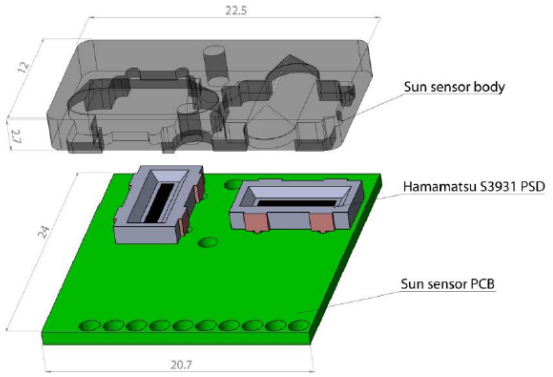

Fig. 17 Sun sensor hardware layout [21]

A PSD consists of a uniform resistive layer formed on one or both surfaces of a high-resistivity semiconductor substrate, and a pair of electrodes for extracting position signals [19]. When light strikes the PSD, an electric charge proportional to the light intensity is generated at the incident position (see figure 14). This electric charge is converted to a photo-current that is collected by the output electrodes X_1 and X_2 [19]. The I_1 and I_2 obtained from the output electrodes can be used to compute the light position x on the PSD using the following equation [20]:

$$\frac{I_2 - I_1}{I_1 + I_2} = \frac{2x}{L} \tag{33}$$

Two-dimensional PSD extend the same principle to two perpendicular axes simultaneously. This section proposes the development of a DSS using two one-dimensional PSDs positioned perpendicularly from each other to replicate the effect of a single two-dimensional PSD. The Hamamatsu S3931 one-dimensional PSD is selected as the baseline component for the customized Sun sensor due to its relatively low cost and small size in addition to its flight heritage in CubeSat missions [21]. The implementation of a one-dimensional PSD requires a slit to be located perpendicular to the orientation of the sensor element as shown on figure 16. Multiple design parameters can be varied to change the FOV and the angle where diffraction effects take place [22]. Researchers of the ESTCube-1 nanosatellite found that the optimal slit width was approximately 0.1 mm and resulted in a FOV of ±45° for a PSD with a length of 6 mm such as the Hamamatsu S3931 [18]. Figure 17 shows the layout of the Sun sensor hardware assembly. The assembly consists of two one-dimensional PSDs positioned perpendicular to each other and covered by a mask containing two slits oriented perpendicular to the corresponding PSDs. The PSDs are soldered to a Printed Circuit Board (PCB) that contains all the electronic components necessary for signal processing. The two main circuits/components needed for signal processing are the following: A Current-to-Voltage (CVC) conversion circuit shown on figure 18 and an Analog to Digital (ADC) Converter, plus any capacitors/resistors necessary to filter the output signal. The CVC circuit used by the ESTCube-1 nanosatellite is shown on figure 19. This circuit includes a Low-Pass-Filter at the outputs to enhance signal characteristics. Analog outputs are converted to digital signals using a Maxim MAX1230 ADC [21]. The ESTCube-1 ADCS system, including the PSD Sun detection system explored in this section, was successfully validated in orbit despite losing one of its six sensors [23]. Following the flight demonstration, ESTCube-1 developers argued that the low

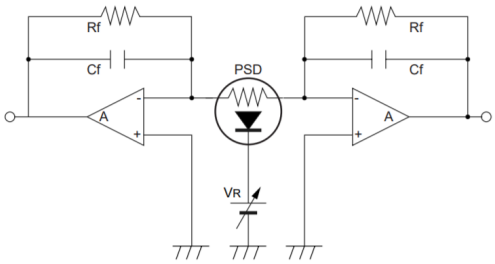

Fig. 18 CVC conversion circuit layout [20]

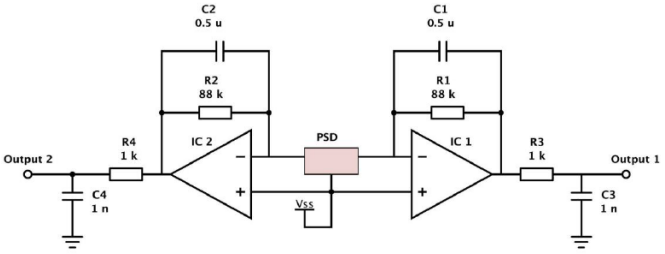

Fig. 19 CVC circuit for ESTCube-1 [18]

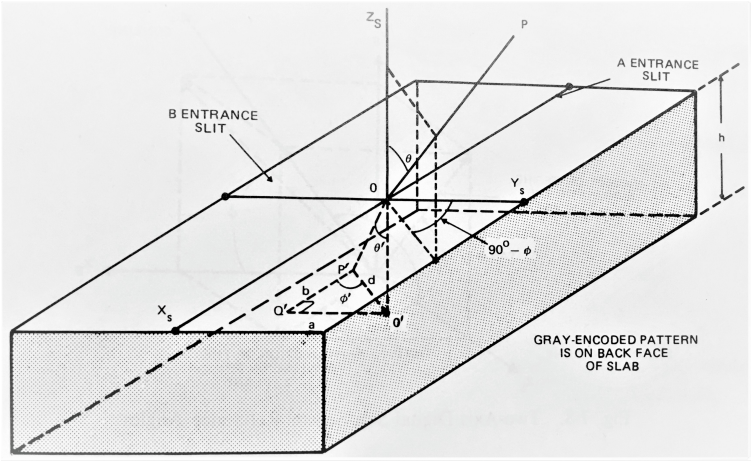

Fig. 20 Two-axis Sun sensor optics [25]

reflectivity of the sensor mask is of great importance in order to prevent non-incident light to reach the PSD. Ideally, any internal light reflection could be avoided with the proper mask design [24]. In addition, developers suggested that increasing the sensor FOV could potentially improve the accuracy of the system despite the increased impact from Earth albedo noise [24].

After the digital signal has been recorded by the computer, azimuth and elevation angles of the Sun in the sensor frame can be computed as follows. Two PSDs (X-PSD and Y-PSD) are aligned with the x and y-axis and are masked by slits B and A respectively. The diagram of a two-axis sun sensor with an incoming Sun vector OP is shown in Figure 20. Two perpendicular one-axis Sun sensor optics can be assumed to perform analogous to figure 20. The light spots passing through each slit (computed with equation 33) are denoted by b and a, and correspond to the X-PSD and the Y-PSD respectively. The light spots b and a can then be used to compute the azimuth (ϕ) and coelevation (θ) angles using equations 34 and 35 [25]:

$$\phi = ATAN2(a, b) \tag{34}$$

$$\theta = arctan\left\{\frac{n(a^2 + b^2)^{1/2}}{\left[h^2 - (n^2 - 1)(a^2 + b^2)\right]^{1/2}}\right\} < \pm 45^\circ \tag{35}$$

ATAN2 is the four-quadrant inverse tangent, h is the height from the slit to the PSD and n is the refractive index ($n = 1$ at vacuum). These assumptions help reduce equation 35 to:

$$\theta = arctan\left\{\frac{(a^2 + b^2)^{1/2}}{h}\right\} < \pm 45^\circ \tag{36}$$

Next, the Sun vector is transformed from the sensor frame to the spacecraft frame using equation 37 [25]:

$$A_{SS} = \begin{bmatrix} -sin\phi - \delta\psi sin\lambda cos\phi & \delta\psi sin\phi - sin\lambda cos\phi & cos\phi cos\lambda \\ cos\phi - \delta\psi sin\lambda sin\phi & -\delta\psi cos\phi - sin\lambda sin\phi & sin\phi cos\lambda \\ \delta\psi cos\lambda & cos\lambda & sin\lambda \end{bmatrix} \tag{37}$$

On the expression above, $\delta\psi$ is a small misalignment angle about the boresight and can be assumed to be zero for simplified sensor models. Finally, the elevation angle (λ) corresponds to $\lambda = 90° - \theta$. Finally, A_{SS} can be used to convert the Sun vector to the spacecraft frame; therefore producing the 3-component Sun vector from a single sensor assembly.

VIII. Acknowledgements

This work would not be possible without the endless support and patience of Dr. Glenn Lightsey. Furthermore, I would like to acknowledge the School of Aerospace Engineering and the Space Systems Design Lab (SSDL) for providing funding for the procurement of the GT-1 launch and spacecraft hardware.

Finally, I would like to thank many students in the SSDL; in particular Chris Carter, Rohan Thatavarthi, Andrew Fear, William Jun and Julian Brew for graciously sharing their ideas and providing open and honest feedback that has allowed this work to evolve and improve just as much as its first author.

References

[1] Norris, S., "Georgia Tech Satellite Successfully Launched Into Space," `https://www.news.gatech.edu/2019/06/25/georgia-tech-satellite-successfully-launched-space`, 2019. Accessed: 2019-12-06.

[2] NASA CubeSat Launch Initiative, "CubeSat 101: Basic Concepts and Processes for First-Time CubeSat Developers," , 2017. October, p. 96.

[3] Springmann, J. C., "Satellite Attitude Determination with Low-Cost Sensors," Ph.D. thesis, University of Michigan, 2013.

[4] Theil, S., Appel, P., and Schleicher, A., "Low cost, good accuracy-attitude determination using magnetometer and simple sun sensor," *17th Annual AIAA/USU Conference on Small Satellites*, 2003.

[5] Appel, P., "Attitude estimation from magnetometer and earth-albedo-corrected coarse sun sensor measurements," *Acta Astronautica*, Vol. 56, No. 1-2, 2005, pp. 115–126.

[6] OSRAM Opto Semiconductors, *SFH2430 DIL SMT Ambient Light Sensor*, OSRAM, Feb 2018. Version 1.3.

[7] Honeywell International Inc, *1, 2 and 3 Axis Magnetic Sensors HMC1051/HMC1052/HMC1053*, Honeywell, Mar 2016. Form #900308 Rev B.

[8] NovAtel Inc, *Receivers OEM615*, NovAtel, Nov 2015. Version 8.

[9] Crassidis, J. L., and Junkins, J. L., *Optimal estimation of dynamic systems*, Chapman and Hall/CRC, College Station, Texas, 2011.

[10] Seiko Epson Corporation, *M-G364PD High Stability IMU*, Epson, Feb 2018. Rev.20180228.

[11] Markley, F. L., and Crassidis, J. L., *Fundamentals of spacecraft attitude determination and control*, Vol. 33, Springer, New York City, New York, 2014.

[12] O'Keefe, S. A., "Autonomous Sun-Direction Estimation Using Partially Underdetermined Coarse Sun Sensor Configurations," Ph.D. thesis, University of Colorado, 2015.

[13] Sityar, I., "Sun sensor implementation using solar power arrays," Master's thesis, NAVAL POSTGRADUATE SCHOOL, 1992.

[14] Crassidis, J. L., and Markley, F. L, "Fundamentals of Spacecraft Attitude Determination and Control," `http://ancs.eng.buffalo.edu/index.php/Fundamentals_of_Spacecraft_Attitude_Determination_and_Control`, 2014. Accessed: 2019-11-10.

[15] Farrenkopf, R., "Analytic steady-state accuracy solutions for two common spacecraft attitude estimators," *Journal of Guidance and Control*, Vol. 1, No. 4, 1978, pp. 282–284.

[16] Schaub, H., "Kinematics: Describing the Motions of Spacecraft," https://www.coursera.org/learn/spacecraft-dynamics-kinematics#syllabus, Aug 2019. Coursera online course notes, Accessed: 2019-08-25.

[17] Simon, D., *Optimal state estimation: Kalman, H infinity, and nonlinear approaches*, John Wiley & Sons, Hoboken, New Jersey, 2006.

[18] Valner, R, "Characterization of Custom Built Sun Sensor for ESTCube-1," , 2013. Bachelor's Thesis, University of Tartu.

[19] Hamamatsu Photonics, "PSD: Position Sensitive Detectors," https://www.hamamatsu.com/resources/pdf/ssd/psd_techinfo_e.pdf, Aug 2013. Accessed: 2020-01-06.

[20] Hamamatsu Photonics, "One-dimensional PSD," https://www.hamamatsu.com/resources/pdf/ssd/s3931_etc_kpsd1002e.pdf, Oct 2017. Accessed: 2020-01-06.

[21] Slavinskis, A., Kulu, E., Viru, J., Valner, R., Ehrpais, H., Uiboupin, T., Järve, M., Soolo, E., Envall, J., Scheffler, T., et al., "Attitude determination and control for centrifugal tether deployment on the ESTCube-1 nanosatellite." *Proceedings of the Estonian Academy of Sciences*, Vol. 63, 2014.

[22] Post, M. A., Li, J., and Lee, R., "A low-cost photodiode sun sensor for CubeSat and planetary microrover," *International Journal of Aerospace Engineering*, Vol. 2013, 2013.

[23] Slavinskis, A., Pajusalu, M., Kuuste, H., Ilbis, E., Eenmae, T., Sunter, I., Laizans, K., Ehrpais, H., Liias, P., Kulu, E., Viru, J., Kalde, J., Kvell, U., Kutt, J., Zalite, K., Kahn, K., Latt, S., Envall, J., Toivanen, P., and Polkko, J., "ESTCube-1 in-orbit experience and lessons learned," *IEEE aerospace and electronic systems magazine.*, Vol. 30, No. 8, 2015, pp. 12–22.

[24] Slavinskis, A., Ehrpais, H., Kuuste, H., Sunter, I., Viru, J., Kutt, J., Kulu, E., and Noorma, M., "Flight results of ESTcube-1 attitude determination system," *Journal of Aerospace Engineering*, Vol. 29, No. 1, 2016.

[25] Wertz, J. R., *Spacecraft attitude determination and control*, Astrophysics and space science library ; v. 73, Reidel, Dordrecht; Boston, 1978.